Langmuir

Article

pubs.acs.org/Langmuir

Role of Mixed Boundaries on Flow in Open Capillary Channels with Curved Air−Water Interfaces

Wenjuan Zheng,[†] Lian-Ping Wang,[‡] Dani Or,[§] Volha Lazouskaya,[†] and Yan Jin*[,†]

[†]Department of Plant and Soil Sciences and [‡]Department of Mechanical Engineering, University of Delaware, Newark, Delaware, United States

[§]Department of Environmental Sciences, Swiss Federal Institute of Technology, Zurich, Switzerland

Supporting Information

ABSTRACT: Flow in unsaturated porous media or in engineered microfluidic systems is dominated by capillary and viscous forces. Consequently, flow regimes may differ markedly from conventional flows, reflecting strong interfacial influences on small bodies of flowing liquids. In this work, we visualized liquid transport patterns in open capillary channels with a range of opening sizes from 0.6 to 5.0 mm using laser scanning confocal microscopy combined with fluorescent latex particles (1.0 μm) as tracers at a mean velocity of ~0.50 mm s^{-1}. The observed velocity profiles indicate limited mobility at the air−water interface. The application of the Stokes equation with mixed boundary conditions (i.e., no slip on the channel walls and partial slip or shear stress at the air−water interface) clearly illustrates the increasing importance of interfacial shear stress with decreasing channel size. Interfacial shear stress emerges from the velocity gradient from the adjoining no-slip walls to the center where flow is trapped in a region in which capillary forces dominate. In addition, the increased contribution of capillary forces (relative to viscous forces) to flow on the microscale leads to increased interfacial curvature, which, together with interfacial shear stress, affects the velocity distribution and flow pattern (e.g., reverse flow in the contact line region). We found that partial slip, rather than the commonly used stress-free condition, provided a more accurate description of the boundary condition at the confined air−water interface, reflecting the key role that surface/interface effects play in controlling flow behavior on the nanoscale and microscale.

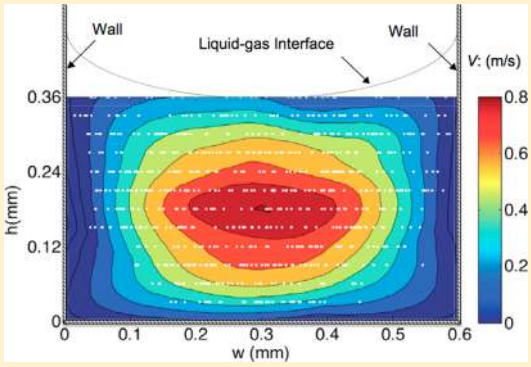

INTRODUCTION

Multiphase flow in porous media is relevant to many natural and industrial processes encountered in soil physics, surface and colloidal sciences, environmental sciences, and petroleum and chemical engineering. Such flow takes place in highly interconnected and tortuous regions bounded by solid−water and air−water interfaces.[1] Although these fluid interfaces are massless, they exert significant influence on the dynamics of multiphase flow by shaping flow pathways and their ability to sustain stress. Simple Darcy-like flux extended from single-phase flow does not always sufficiently capture the physics of flow in processes such as water flow in partially saturated soil or oil extraction from a reservoir.[2] Alternatives based on mass, momentum, and energy conservation laws have been proposed to provide more accurate descriptions of multiphase flow by coupling conservation equations associated with phases and interfaces.[3] These descriptions require an adequate understanding of pore-scale flow and the interfacial processes and conditions that control the flow.

Pore-scale flow is strongly influenced by the relatively large interfacial areas (per unit volume) where surface tension, viscosity, and diffusion processes dominate gravity and inertia.[4,5] In multiphase flow systems, the air−water interface is bounded ubiquitously by adjoining solid surfaces. This study focuses on the boundary condition for water at the air−water interface. It is argued that the description of the boundary condition at the air−water interface is of relatively little consequence because of the strong constraint from no-slip walls.[6] However, other studies that considered flow on surfaces with similar mixed boundaries indicated that the air−water interface affected the overall mobility of water bounded by mixed interfaces.[7−9] Therefore, as a key component of the mixed boundaries, the boundary condition at the air−water interface requires an accurate characterization and description.

In general, a clean air−water interface on the macroscopic or continuum scale is often treated as a full-slip or stress-free boundary.[6,8,10,11] Although some experimental results seem to provide supportive evidence for this assumption,[12,13] others indicate different types of boundary conditions, such as partial slip or even no slip.[12,14−17] In addition to the inconsistencies in the types of boundary conditions at the air−water interface, there are also uncertainties as to the physical mechanisms responsible for preventing the air−water interface from being stress-free. The presence of minor impurities in the experimental systems was suspected as the cause of the

Received: December 5, 2011
Published: August 6, 2012

observed partial-slip boundary condition in several studies.[15,18] However, the partial-slip boundary was also observed in very clean systems.[14,17] Manor et al.[15,18] reported, on the basis of their atomic force microscopy study using a 50-μm-radius bubble in a clean system (i.e., in an electrolyte without surfactant), that the air−water interface did not obey the stress-free boundary condition. Lazouskaya et al.[17] demonstrated that the air−water interface in an open rectangular capillary channel had limited mobility (i.e., it was not stress-free) and could be described by a partial-slip boundary condition. Therefore, the physical origin of interfacial shear stress and the resulting partial-slip boundary condition in clean systems remains poorly understood.

Another factor that influences the microscopic behavior of multiphase flow is the shape of the air−water interface. When water is confined within small pores, the air−water interface is curved rather than flat because of the increasing capillary pressure at decreasing scales. The impact of meniscus shape on fluid flow has been discussed in the literature.[11,19−22] Ransohoff and Radke[19] reported that an increasing contact angle diminished the available area for flow and thereby caused a greater resistance to flow. Such a curved air−water interface can also induce additional energy dissipation as compared to that of a flat interface, resulting in a lower effective slip length.[7,8,23]

The growing interest in microfluidic technology and advances in computational and observational methods now enable the resolution of micrometric flow processes. Boundary conditions can be deduced indirectly by measuring forces between surfaces and interfaces using, for example, a surface force apparatus (SFA)[24] or atomic force microscopy (AFM)[15,25] or determined directly using microparticle image velocimetry (μ-PIV).[17,26] Since its introduction by Santiago et al.,[27] the μ-PIV method has become a standard tool for measuring fluid velocity in microfluidic devices for near-wall flow, single-phase and multiphase flow, steady and turbulent flow, and pressure-driven, surface-tension-driven, and electrokinetic flow.

This work extends our previous research on air−water interfacial behavior in capillary channels[17] by examining the physical origin of the observed limited mobility of the small-scale air−water interface. Particle tracking by means of confocal microscopy enabled the experimental determination of air−water interfacial shapes and flow velocity profiles in open rectangular microchannels with a range of opening sizes (0.6−5.0 mm). The results were compared with theoretical analyses that examined the influence of the air−water interfacial shape and boundary conditions on the flow pattern in open-square channels.

THEORETICAL CONSIDERATIONS

Meniscus Shape between Two Vertical Walls. We employed two approaches to calculate the meniscus shape of an air−water interface confined between two vertical walls with spacing ranging from 0.1 to 5.0 mm. The first approach involved the calculation of the exact meniscus shape under static conditions by balancing gravitational and capillary pressures (Supporting Information, S1)

$$\rho g(h - h_0) = \frac{\sigma \frac{d^2h}{dx^2}}{\left[1 + \left(\frac{dh}{dx}\right)^2\right]^{3/2}} - \frac{2\sigma \cos\theta}{w} = \frac{\sigma}{R} - \frac{\sigma}{R_0} \tag{1}$$

where x is the distance measured horizontally from one wall of the channel (m), h is the local height of water (m), ρ is the density of the bulk phase (kg m^{-3}), σ is the surface tension (N m^{-1}), and R is the local radius of curvature (m). The reference radius of curvature is defined as $R_0 = w/(2\cos\theta)$, which is the radius of a circle passing through the two contact points on the vertical walls with the prescribed contact angle θ between the liquid and the vertical walls. w is the width of the channel (m). The reference height h_0 represents the average height (m) (measured from the bottom of the channel) of the meniscus or, equivalently, the height of the air−water interface if the interface is flat. The boundary conditions on the vertical walls (i.e., $x = 0$) satisfy

$$\left.\frac{dh}{dx}\right|_{x=0} = -\frac{1}{\tan\theta} \tag{2}$$

Because we assume that the two vertical boundary walls are identical, the meniscus shape is symmetric about $x = {}^{w}/_{2}$; therefore,

$$\left.\frac{dh}{dx}\right|_{x=w/2} = 0 \tag{3}$$

and only half of the meniscus (from $x = 0$ to ${}^{w}/_{2}$) needs to be computed.

The second approach calculates the meniscus shape neglecting the gravity effect and assuming a constant mean curvature for the whole interface (i.e., a circular meniscus). The mean curvature depends on the contact angle between the liquid and the wall. The meniscus shape based on this approach is

$$h = h_0 - \sqrt{\left(\frac{w}{2\cos\theta}\right)^2 - \left(x - \frac{w}{2}\right)^2} + \frac{w}{2\cos\theta}\left[\frac{\sin^{-1}(\cos\theta)}{2\cos\theta} + \frac{1}{2}\sin\theta\right] \tag{4}$$

In fact, eq 4 can be derived from eq 1 by simply setting the left-hand side of eq 1 equal to zero (Supporting Information, S2). Namely, eq 4 represents a limiting-case solution of eq 1 when w approaches zero or under a microgravity condition, and as such the capillary force completely dominates the entire air−water interface.

In general eqs 1−3 were solved numerically, and the solution was compared to that of eq 4. When the spacing between two vertical walls increases, the interfacial curvature at the center position decreases when other parameters are kept constant. This indicates the increasing influence of body forces such as gravity relative to the capillary force on the meniscus shape. Therefore, by comparing the exact meniscus shape calculated from eq 1 with the approximation assuming the meniscus to be a circular arc (eq 4), we can infer the importance of the capillary effect in the system.

Flow in Open Capillary Channels. We considered the steady-state motion of an incompressible viscous fluid through a straight microchannel. For 1D flow in the z direction (Figure 1), the inertial term is identically zero. The flow is governed by the balance of the pressure gradient and the viscous term, namely, the Stokes equation[28]

$$\nabla^2 v = \frac{1}{\mu}\frac{dp}{dz} \tag{5}$$

dx.doi.org/10.1021/la302833p | Langmuir 2012, 28, 12753−12761

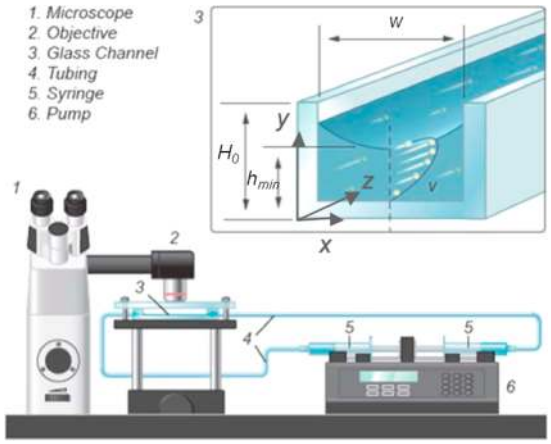

Figure 1. Schematic diagram of the experimental setup.

where v is the velocity component in the z direction (m s^{-1}), μ is the viscosity (N s m^{-2}) of the bulk phase, and dp/dz is the pressure gradient along the channel (Pa m^{-1}).

The no-slip boundary condition is commonly applied at the solid–water interface as[28]

$$v = 0 \tag{6}$$

At the air–water interface, the boundary condition is described in the following form[21]

$$\mu \nabla v \cdot \hat{n} = \tau_0 \tag{7}$$

where $\hat{n}$ is the unit outward normal to the interface and τ_0 is the interfacial shear stress (N m^{-2}) that acts in the direction opposite to the direction of the bulk liquid flow. Mathematically, $\tau_0 = 0$ represents a stress-free surface whereas $\tau_0 < 0$ corresponds to a partial-slip boundary.

The Stokes equation (eq 5) was applied to model measured flow velocity profiles in the experimental microchannels, where the air–water interfaces were not pinned at the edges and did not reach the channel bottoms (Figure 1). The cross-sectional liquid-filled area was assumed to be rectangular by neglecting the flow in the contact line region. As a result, the partial differential equation over a rectangular domain can be solved analytically by the separation of variables. The following dimensionless variables were introduced: $u = -v\mu/w^2\,(dp/dz)$, $X = x/w$, and $Y = y/h$. Under this scaling, the governing equation (eq 5) and boundary conditions (eqs 6 and 7) have the form

$$\frac{\partial^2 u}{\partial X^2} + s^2 \frac{\partial^2 u}{\partial Y^2} = -1 \tag{8}$$

$$u|_{X=0} = 0 \tag{9}$$

$$u|_{X=1} = 0 \tag{10}$$

$$u|_{Y=0} = 0 \tag{11}$$

$$\left.\frac{du}{dY}\right|_{Y=1} = \tau \tag{12}$$

where $s = w/h$ is the aspect ratio and $\tau = (\tau_0 h)/(w^2(-dp/dz))$ is the dimensionless form of the interfacial shear stress.

The analytical solution of the above equations is

$$u(X, Y) = -\frac{X^2}{2} + \frac{X}{2} + \sum_{i=1}^{n} \sin(n\pi X)\left\{ \frac{2((-1)^n - 1)}{(n\pi)^3} \cosh\left(\frac{n\pi Y}{s}\right) + \frac{\frac{2((-1)^n - 1)}{(n\pi)^3}\left[\sinh\left(\frac{n\pi}{s}\right) + \tau s(n\pi)\right]}{\cosh\left(\frac{n\pi}{s}\right)} \sinh\left(\frac{n\pi Y}{s}\right) \right\} \tag{13}$$

By fitting eq 13 to experimentally measured velocity profiles at the channel center, $x = {}^{w}/_{2}$, two parameters that characterize the interfacial and flow properties (i.e., the interfacial shear stress and pressure gradient) were obtained. The computation was performed using a least-squares fitting procedure.

We also examined the effects of different types of boundary conditions at the air–water interface on the cross-sectional flow pattern. When unidirectional flow through an open-square microchannel was considered, the velocity distribution was calculated by solving eqs 5–7 by assuming a flat air–water interface. The governing equation was set as $\nabla^2 u = 1$, and the boundary conditions at the open surface were $u = 0$, $\tau = -0.2$, and $\tau = 0$ representing no-slip, partial-slip, and stress-free conditions, respectively. In addition, we considered flow pattern with a curved air–water interface subjected to the above boundary conditions. The curvature κ, the reciprocal of the interfacial arc radius, was arbitrarily set to 1.6. The unit square domain in transformed variables X and Y was chosen because the Stokes equation solved over a rectangular area can be reduced to a dimensionless form over a unit square domain. The partial differential equation (eq 8), together with the boundary conditions (eq 9–12), was solved numerically using the "pdetool" toolbox in Matlab.

EXPERIMENTAL MATERIALS AND METHODS

Experimental Setup. A schematic representation of the experimental setup is given in Figure 1. The confocal laser scanning microscope μ-PIV system (Zeiss 5 LIVE DUO, Carl Zeiss, Oberkochen, Germany) consisted of an inverted microscope, a confocal scanning unit, a laser with an excitation wavelength of 488 nm, and a high-speed camera. This system has the capability to acquire a series of in-focus images by means of depth-wise optical slicing, allowing 3D image reconstruction.[29] Two air-immersion objective lenses with magnifications of 10× and 5× and corresponding numerical apertures of 0.3 and 0.25, respectively, were used. A more detailed description and working principles of the μ-PIV system can be found in another reference.[30]

Rectangular Glass Microchannels. The open microchannels were made from rectangular glass tubing (Friedrich & Dimmock Inc., Millville, NJ), which was cut lengthwise and embedded into a waxy base. Five microchannels with different inside dimensions ($w \times H$) of 0.60 mm × 0.42 mm, 1.00 mm ×0.70 mm, 2.00 mm × 1.60 mm, 3.00 mm × 2.60 mm, and 5.00 mm × 4.40 mm were used. The opening length of the microchannels was 40 mm in the axial direction for all channels except the 5.0 mm, which was 100 mm long. The lengths were selected to allow flow to develop fully in the channels. The inlet and outlet of the microchannel were connected directly to a precision syringe pump (PHD, Harvard Apparatus, Holliston, MA) using plastic tubing. The microchannels were reused for repeated experiments after a thorough cleansing, following the procedure described by Lazouskaya et al.[17]

Working Fluid and Tracers. The working fluid was deionized water seeded with 1.0-μm-diameter fluorescent particles (Molecular Probes Inc., Eugene, OR) as flow tracers. The particles were

dx.doi.org/10.1021/la302833p | Langmuir 2012, 28, 12753–12761

carboxylate-modified, hydrophilic, yellow-green, surfactant-free latex microspheres with a mass density of 1.055 g cm^{-3}, which is close to the density of water such that the gravitational force is balanced by the buoyancy force. We used a dilute particle suspension of 1 ppm concentration (i.e., 1.4×10^6 particles mL^{-1}) in all experiments. To ensure a monodisperse state, both concentrated and dilute colloidal suspensions were sonicated in an ultrasonic bath (Ultramet, Buehler, Lake Bluff, IL) for 1 min before use.

To examine whether the addition of colloid tracers would change the solution surface tension, we measured the surface tension of suspensions (0.16 mM $NaHCO_3$) at different colloid concentrations of 0, 2, 4, 6, 8, and 10 ppm using the du Noüy ring method with a KSV sigma 700 tensiometer (KSV Instruments Ltd., Helsinki, Finland). All measurements were performed at room temperature (20 °C). The measurements gave an average surface tension of 7.19×10^{-2} N m^{-1} with a small standard deviation of 9.33×10^{-5} N m^{-1}, which indicates that the addition of colloids did not alter the solution surface tension.

μ-PIV Experimental Protocol. We conducted a series of flow experiments at a mean velocity of ~0.50 mm s^{-1}. Optically sectioned images were captured along the y axis (Figure 1) at a step size of either 50 or 100 μm at a resolution of 512 pixels × 512 pixels with a 12-bit gray scale and a scan rate of 20 frames s^{-1}. The objective lens focused on the middle between the inlet and outlet of the channels. Particle tracking software Volocity 5′ (PerkinElmer Inc., Waltham, MA) was used to analyze the images to calculate the particle velocities and construct the velocity profiles. The location of the channel center $x = {}^{w}/_{2}$ (Figure 1) was estimated by applying a quadratic equation to the measured velocity profiles along the x axis at each layer to overcome the difficulties in directly determining the positions of microchannel walls from the images. Location $x = {}^{w}/_{2}$ acquired using this method was extended to the top layer (air−water interface: $y = h$). The velocity on the bottom layer (liquid−solid interface: $y = 0$) was assumed to be 0 (i.e., no slip).

To ensure steady-state flow, images were captured approximately 30 min after the initiation of each experiment when the configuration and position of the air−water interface remained unchanged over the observation time spans. Evaporation, which has been identified as a source of potential error (e.g., inducing the Marangoni effect, changing mass balance, etc.),[31] was minimized by placing the microchannel inside a closed chamber packed with moist sponges during each experiment.

Visualization of Air−Water Interfacial Shape. We also conducted experiments to characterize the static air−water meniscus shape using the same experimental setup shown in Figure 1. Rhodamine B isothiocyanate (Sigma-Aldrich, St. Louis, MO) was added to the working fluid to improve the imaging quality of the interface. Three-dimensional configurations of air−water interfaces were built from stacks of 2D images with a section depth of 8.17 μm for 0.6 mm and 2.0 mm channels and 40.3 μm for the 5.0 mm channel, respectively.

RESULTS

We present results from a large number of captured confocal images that were analyzed for particle velocities to provide quantitative flow-field descriptions in the microchannels. Figure 2 is a representative transverse 2D velocity map, constructed for the 0.6 mm channel with a mean velocity of 0.514 mm s^{-1}, showing that the air−water interface was mobile and the maximum velocity was located in the middle of the channel. This finding indicates that the air−water interface was not stress-free. It should be noted that although the liquid was flowing with a curved interface (Figure 3) the velocity distribution was measured for a rectangular area by neglecting the contact line regions where we observed flow reversal. (Movie 1 is given in the Supporting Information, showing colloid tracers in the contact line region moving in the direction opposite to the bulk flow.)

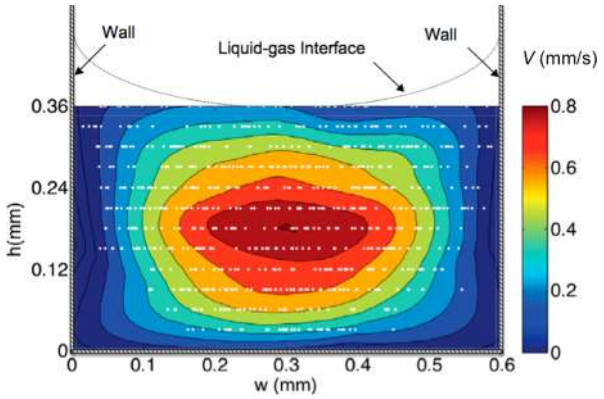

Figure 2. Representative 2D velocity distribution profile measured in the 0.6 mm channel at a mean velocity of 0.514 mm s^{-1}.

The flow pattern and interface characteristics were further examined through 1D velocity profiles (Figure 4) constructed on the basis of velocities measured at the center of each of the five microchannels, ranging in size from 0.6 to 5.0 mm. These profiles all have similar shapes and, to some extent, resemble Poiseuille flow, a typical flow pattern found in fully developed incompressible flow in a closed capillary conduit. However, unlike Poiseuille flow, the profiles are not completely symmetrical from the solid−water interface (at the channel bottom) to the air−water interface because the velocities did not vanish at the air−water interface. For a given mean flow rate, although velocities at the air−water interface in different channels were not significantly different, the maximum velocity in the profile decreased with increasing channel size from 0.88 mm s^{-1} (0.6 mm channel) to 0.65 mm s^{-1} (5.0 mm channel). In addition, the position of the maximum velocity shifted closer to the interface with increasing channel size.

We calculated velocity profiles for the same channel dimensions by solving the Stokes equation (eq 5) assuming a partial-slip boundary condition (eq 7, $-\infty < \tau < 0$) at the air−water interface, fitted the solutions (eq 13) to experimentally measured profiles, and estimated surface shear stress values and the pressure drop for each channel (Table 1). The theoretical and experimental velocity profiles matched very well (Figure 4). In addition, for the same mean flow rate, the value of the dimensionless interfacial shear stress increased (i.e., became more negative from −0.059 to −0.136) as the channel size decreased from 2.0 to 0.6 mm whereas it remained relatively constant for 2.0, 3.0, and 5.0 mm channels (Table 1). Furthermore, the fitted pressure drop across each channel increased (i.e., became more negative from −0.8 to −59.8) as the channel size decreased (Table 1). These results indicate that the interfacial shear stress and thus the air−water interface mobility are functions of the channel size.

Our measurements confirm that the air−water interface confined in small channels was curved rather than flat (Figure 3). Experimentally determined interfacial shapes for channel sizes of 0.1, 0.6, 2.0, and 5.0 mm were in reasonable agreement with calculated values using eq 1 with σ = 72.2 m J m^{-2}, ρ = 1000 kg m^{-3}, g = 9.8 m s^{-2}, and $\theta = 14°$. Moreover, for small channels with sizes of ≤2.0 mm ($Bo \leq 0.144$), the interface shapes are similar to those approximated on the basis of circular arcs of equal size (eq 4). However, for larger channels with sizes >2.0 mm, the interfacial curvature decreased along the interface receding from the wall.

dx.doi.org/10.1021/la302833p | Langmuir 2012, 28, 12753−12761

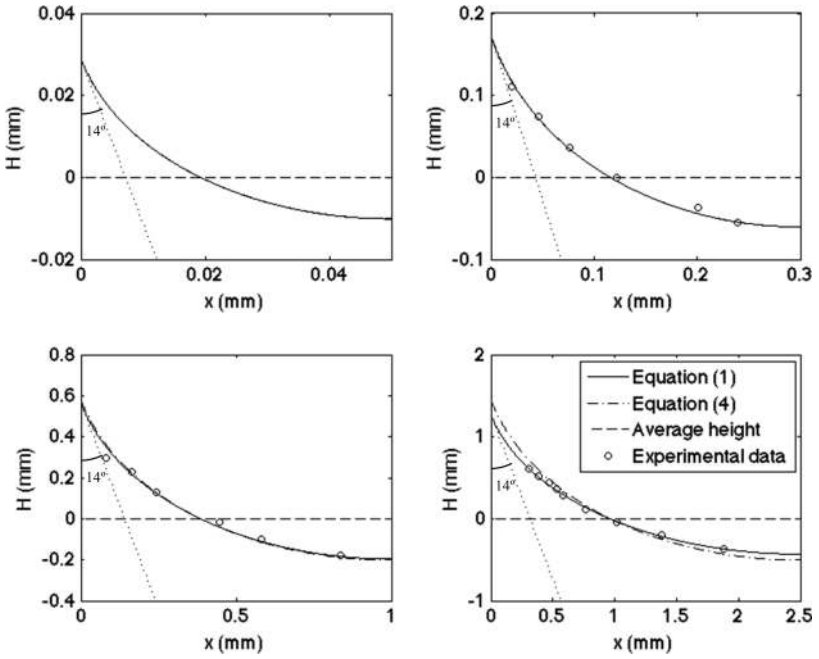

Figure 3. Calculated meniscus shapes for water confined between two vertical glass plates with spacings of 0.1, 0.6, 2.0, and 5.0 mm and measured air−water interface shapes in 0.6, 2.0, and 5.0 mm channels ($0 \le x \le {}^{w}/_{2}$). Note that $H(x) = h(x) - h_0$, where $h(x)$ is the meniscus shape function.

To evaluate the effect of boundary conditions and interfacial shape on the flow characteristics in open microchannels, we performed theoretical calculations of 2D velocity distributions over a unit square domain for a flat (Figure 5a−c) and a curved air−water interface (Figure 5d−f) with an arbitrary curvature of $\kappa = 1.6$ for three boundary conditions at the air−water interface: no slip, partial slip, and stress free, respectively. Our analysis shows that the maximum normalized velocities were higher in channels with a flat air−water interface at 0.073, 0.082, and 0.114 for the three boundary conditions, respectively, than the corresponding values with a curved interface at 0.038, 0.043, and 0.060. The increased shear stress associated with a curved interface decreased the maximum flow velocity as well as lowered the location (i.e., was closer to the channel bottom) where the maximum velocity was measured. Figure 5e, calculated for flow with a curved air−water interface and a partial-slip boundary condition, resembled most closely the experimentally measured 2D velocity map (Figure 2).

Additional calculations compared the effect of interfacial shear stress (τ) and curvature (κ), respectively, on the velocity profile in the center of the channel (Figure 6). The results clearly show that by changing the boundary condition from stress-free to partial slip and then to no slip (i.e., $\tau = 0$, −0.05, −0.1, and −0.2 and $u = 0$) the velocity profile changes its pattern from half parabolic to partially parabolic (the case similar to our experimental observation) and to parabolic (Figure 6a; $\kappa = 0$), demonstrating how interfacial shear stress causes a significant change in the flow field in an open capillary channel. However, at a given shear stress value ($\tau = -0.2$), a change in interfacial curvature had no significant impact on the velocity profiles, and they essentially overlapped with each other (Figure 6b, $\kappa = 0$, 1.6, 1.9, and 1.97).

DISCUSSION

Partial Slip Air−Water Interface and Origin of Interfacial Shear Stress. The air−water interface has, in general, been treated as a stress-free boundary when modeling two-phase flow because the density and viscosity of air are much lower than those of water. Our directly measured velocity profiles in open capillary channels suggest that the interface is not stress-free and is better represented by a partial slip boundary condition. Similar results in various experimental settings (e.g., open capillary channels, air bubbles, and moving meniscus) have been reported by others.[15−18]

The rigidity or limited mobility of air−water interfaces can result from surface tension gradients or the spatial variation of surface energy due to one or more mechanisms.[32] The presence of minor impurities in experimental systems could lead to a partial-slip or even a no-slip boundary condition at air−water interfaces.[15] The addition of colloidal tracers to the fluid could be a potential source of interfacial contamination causing alterations in the interfacial rigidity in our study. However, surface tension measurements of colloidal suspensions at various concentrations (0 to 10 ppm) did not show surface tension changes in these samples. Additionally, our results and the derived interpretation of the effects of channel size on interfacial mobility would not be affected even if the added colloidal tracers slightly varied the fluid properties because the same tracer fluids were used in all experiments.

Our finding that interfacial shear stress increases with decreasing channel size suggests that air−water interfaces in small confined regions cannot be treated as entirely isolated from their surrounding no-slip solid−water interfaces and three-phase contact lines. In the capillary channels used in our study, the air−water interface near a channel wall tends to be stationary whereas it attains a larger velocity away from the wall. This lateral velocity gradient across from the channel wall to its center has to be balanced by a tangential hydrodynamic stress, which gives rise to finite shear stress at the interface.[33] As the spacing between confining walls decreases, the gradient increases and thus leads to larger interfacial shear stress. The dependence of the interfacial behavior of an air−water interface on its proximity to a solid surface has been speculated on or demonstrated in earlier studies.[14,17] In particular, Chan et al.[14]

dx.doi.org/10.1021/la302833p | *Langmuir* 2012, 28, 12753−12761

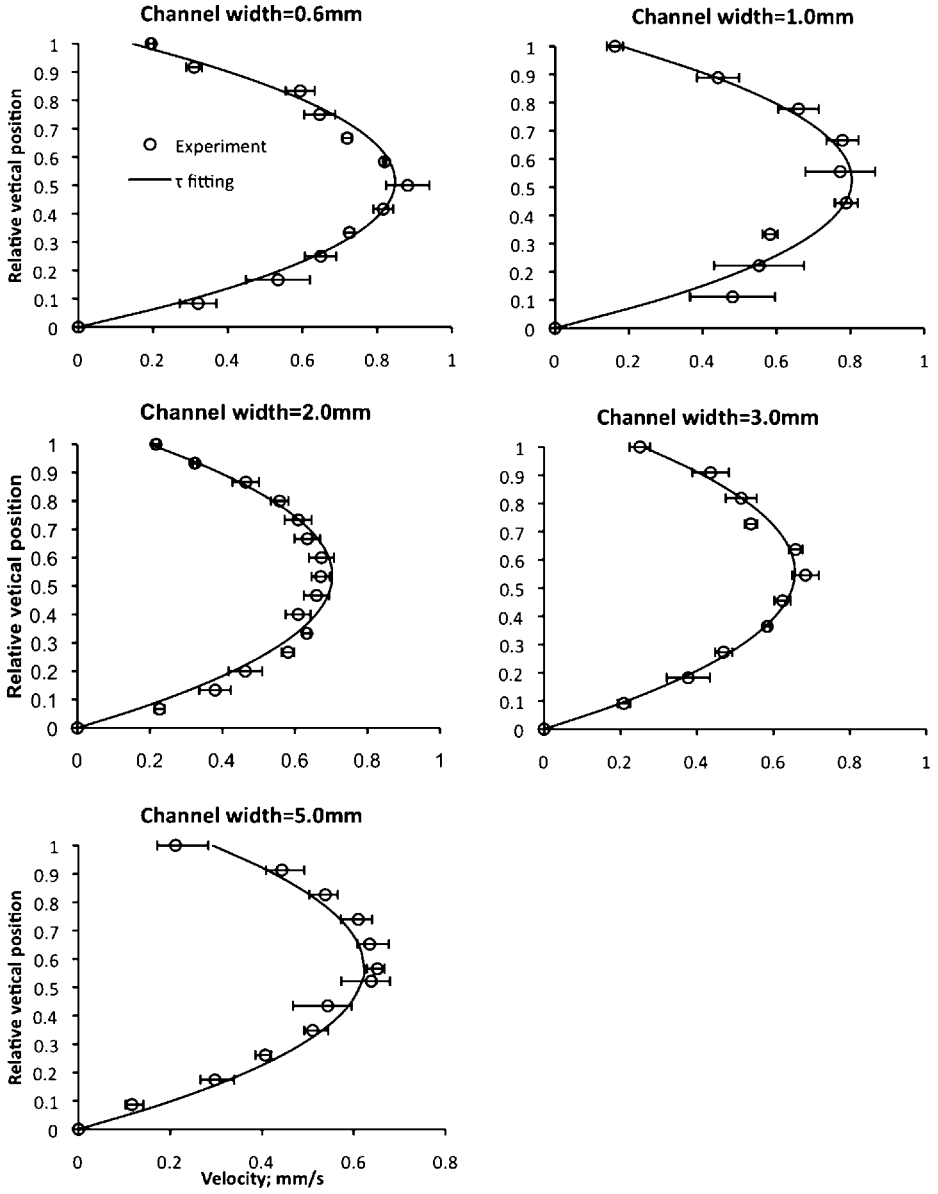

Figure 4. Experimental and theoretical fitted velocity profiles in the middle of the 0.6, 1.0, 2.0, 3.0, and 5.0 mm channels (mean velocity ≈ 0.5 mm s^{-1}). The *y* axis shows the relative vertical position, which is the measurement location normalized by the water height. The error bars are based on three repeated runs.

Table 1. Experimental Conditions and Fitted Parameters

w (mm)	H_0 (mm)[a]	h_{min} (mm)[b]	H_{min}/w	τ	dp/dz (Pa m^{-1})
0.6	0.42	0.36	0.600	−0.136	−59.847
1.0	0.70	0.45	0.450	−0.083	−31.755
2.0	1.60	0.75	0.375	−0.059	−9.264
3.0	2.60	1.10	0.367	−0.054	−3.750
5.0	4.40	2.30	0.460	−0.075	−0.828

[a] H_0: height of the channel (mm). [b] h_{min}: height of filled water at the center of the channel (mm).

reported that a bubble's air−water interface was stress-free when the bubble was far away from a TiO_2 substrate and became more rigid as it approached the substrate.

In addition to channel size, the fitted shear stress also depends on the interfacial curvature, which affects both the cross-sectional area and proportion of the air−water interface in the total length of mixed boundaries. As the channel size decreases, the interfacial curvature and shear stress increase simultaneously, making it very difficult to differentiate their individual contributions to the increased interfacial shear stress. However, the variation of fitted interfacial shear stress for differently sized channels was not expected to be due to the difference in interfacial curvature for two reasons. First, for channels with sizes of <3.0 mm, the interfacial curvatures were all similar to circular arcs (Figure 3). Second, the cross section used for fitting interfacial shear stress was assumed to be rectangular where the air−water interface was flat. The overlapping velocity profiles with different interfacial curvature values ranging from flat to κ = 1.6 (Figure 6b) further indicate that neglecting the interfacial curvature was not the cause of the size effect on the interfacial shear stress.

Although the increased interfacial shear stress with decreasing size for channels with <3.0 mm width was likely caused by the confinement of the no-slip walls, it remained relatively constant for the larger channels (Table 1). This

dx.doi.org/10.1021/la302833p | *Langmuir* 2012, 28, 12753−12761

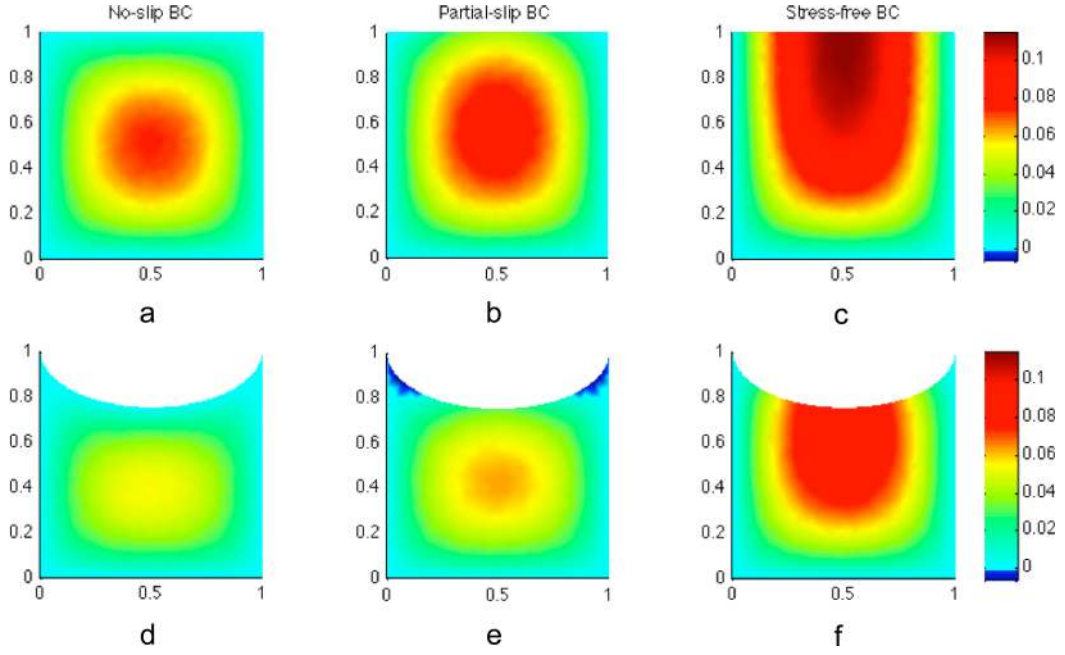

Figure 5. Two-dimensional velocity distribution obtained by solving equation $\nabla^2 u = 1$ over a unit square domain for (a−c) a flat and (d−f) a curved surface with a curvature of 1.6. Boundary conditions applied at the interface were $u = 0$, $\tau = -0.2$, and $\tau = 0$ for the no-slip, partial-slip, and stress-free cases, respectively.

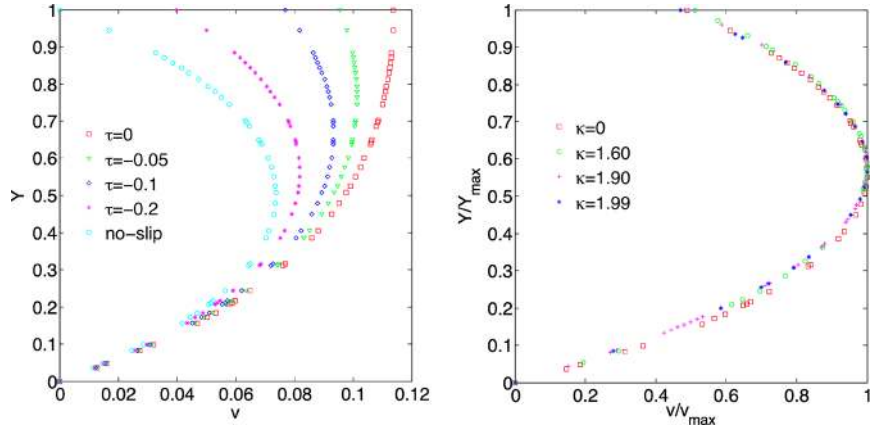

Figure 6. Theoretical velocity profiles at the center of the channels obtained by solving equation $\nabla^2 u = 1$ over a unit square domain under different shear stresses ($\tau = 0$, −0.05, −0.1, and −0.2 and $u = 0$; $\kappa = 0$) and interfacial curvatures ($\kappa = 0$, 1.6, 1.9, and 1.97; $\tau = -0.2$).

Table 2. Dimensionless Numbers

w (mm)	a (mm)[a]	v_m (mm s^{-1})	Ca[b]	Bo[c]	Re[d]	Pe[e]	B[f]
0.6	0.16	0.514	7.35×10^{-6}	0.013	0.084	1458	2.557
1.0	0.24	0.494	7.06×10^{-6}	0.036	0.116	1400	1.772
2.0	0.43	0.463	6.62×10^{-6}	0.144	0.197	1312	1.320
3.0	0.63	0.505	7.22×10^{-6}	0.324	0.319	1432	0.842
5.0	1.20	0.483	6.90×10^{-6}	0.901	0.576	1369	0.644

[a]Characteristic length of the channel (mm), $a = wh/(2h + w)$. [b]Capillary number $Ca = (v_m\mu)/\sigma$. [c]Bond number $Bo = (\rho g w^2)/(4\sigma \cos^2 \theta)$. [d]Reynolds number $Re = (a v_m \rho)/\mu$. [e]Peclet number $Pe = (2r v_m)/D_0$, where D_0 is the diffusion coefficient of particles with radius r(m) and $D_0 = (kT)/6\pi\mu r$, where k is the Boltzmann constant and T is the temperature. [f]Boussinesq number $B = \mu_s/((\mu_1 + \mu_2)w) = 1/M$, where μ_s is the interfacial viscosity (N s^{-1}) and μ_1 and μ_2 are the viscosities of neighboring phases (i.e., liquid and gas (N s m^{-2})). The viscosity of the gas phase is neglected in this system.

suggests that the physical origin of interfacial shear stress is likely different in small and large channels.[34] To compare the competing physical phenomena, we calculated dimensionless numbers (Ca, Bo, Re, and Pe) for all experiments (Table 2). Especially insightful is the Bond number (Bo), which compares the relative contribution of gravitational and capillary forces in affecting flow behavior in differently sized channels. The calculated Bo values increased as the channel size increased, indicating that capillarity dominates only on small scales and that on large scales gravity makes a considerable contribution and therefore cannot be ignored. The calculation of meniscus shapes shows that for channel sizes of <2.0 mm the capillary

dx.doi.org/10.1021/la302833p | Langmuir 2012, 28, 12753−12761

force dominated and for larger channels with sizes >2.0 mm the interfacial curvature was affected by both capillarity and gravity. The commonly used criterion for distinguishing between small and conventionally sized channels in engineering applications is 3 mm.[35] This coincides with the results from the calculation of meniscus shapes as well as the interfacial shear stress fitted by experimental data, where the interfacial shear stress increased as the channel size decreased when the channel size was less than 3 mm. The shape of the cross section, the roughness of the channel walls, and the presence of bends or a small disturbance at the entrance were proposed as possible causes of unequalized shear stresses on both sides of the channel and of the maximum velocity below the surface.[36] This has also been observed in open water systems such as rivers and streams, where the maximum flow velocity often occurs at $\sim^1/_3$ depth below the water surface,[37,38] with a typical flow profile similar to that in Figure 5b.

Flow Pattern Affected by Interfacial Shear Stress. The importance of whether fluid−fluid interfaces during flow in porous media are rigid or mobile has been discussed in the context of flow and transport in porous media.[6,39,40] It has been suggested that finite velocities exist at fluid−fluid interfaces and that they affect the macroscopic permeability of the media.[39] Our study provides experimental evidence that, for flow with mixed boundaries where the air−water interface is bounded by no-slip solid surfaces, the boundary condition at the air−water interface would likely change with the pore size to become more rigid as the pore size decreases. Our results suggest that treating the interface as stress-free would lead to an overestimation of macroscopic permeability.

We show in this study that both the boundary condition (interfacial shear stress) and interfacial curvature affect two-phase flow and transport. Flow resistance β (or friction factor), defined as[11,19]

$$\beta = \frac{w^2}{\mu v_m}\left(-\frac{dp}{dz}\right) \tag{14}$$

where v_m is the mean flow velocity (m s^{-1}), is frequently used to characterize flow efficiency in systems such as capillary or microfluidic channels. This relationship indicates that the flow resistance increases with decreasing mean flow velocity, which is in turn controlled by the interfacial shear stress. In microchannels where the surface area to volume area ratio is large, interfacial shear stress contributes to increased flow resistance and leads to a decreased effective slip length.[21] Interfacial shear stress is therefore considered to be an important parameter in the design of micro- and nanofludic channels. For example, by making channel surfaces rough (i.e., making them superhydrophobic by trapping air and creating air−water interfaces), flow resistance can be reduced and the effective slip length can be increased. Numerical simulations of the effective slip length have been found to overestimate the total effective slip length.[11,34] The overestimation has been attributed to treating the air−liquid interface as flat, thus neglecting interfacial curvature. Our analysis suggests that treating the interface as stress-free and thus ignoring the interfacial shear stress may be another source of overestimation in previous studies.

The observed reverse flow (i.e., the direction of flow is opposite that of bulk flow) in the contact line region also likely resulted from the interfacial shear stress that originated from adjoining channel walls. This conclusion is consistent with our theoretical analysis where reverse flow along the contact lines was generated by solving the Stokes equation with a partial slip boundary and a curved interface (Figure 5e), indicating that the generation of reverse flow can be a direct result of altered interfacial shear stress at a curved interface. By imposing different values of the interfacial shear stress on flow in a wedge, Su et al.[26] showed the occurrence of reverse flow near the interface when shear stress was opposing the flow direction. The phenomenon of reversed flow in the contact line region has been reported in the literature, which was attributed to asymmetric flow around the gas phase or a Marangoni[17] effect due to local variations in the interfacial tension or temperature. Although the possibility of thermal Marangoni flow due to heat emanating from the microscope could not be completely ruled out, this effect was likely very small because of the short duration of the experiments. Our results indicate that the combination of interfacial shear stress and curvature, both characteristics of microscale flow, are the two essential factors that can give rise to the reverse flow phenomenon.

SUMMARY

We examined the boundary condition at the air−water interface and flow pattern on the microscopic scale in capillary channels that are representative of small isolated flow regions found in natural porous media. Experimentally measured velocity profiles showed that the air−water interface possesses some degree of rigidity that increases with increasing flow confinement (i.e., decreasing channel size). The observations can be described by the Stokes equation by invoking a partial-slip boundary condition at the air−water interface. The dominant effect of capillary forces in confined flow regions leads to the observed interfacial curvature and shear stress, which in turn lead to the non-stress-free air−water interface. These results suggest that conservation-based pore-scale models of multiphase flow that treat the air−water interface as wholly isolated from the surrounding solid−water interfaces (i.e., stress-free) would overestimate the flow rate in porous media. Therefore, a partial-slip boundary condition should be considered in describing the free air−water interface taking into account the effects from adjoining solid−water interfaces and the complex flow pattern in the contact line regions in microscale flow where the capillary force dominates. In addition, our study provides a new explanation for the reported overestimation of the slip length in microfluidic channels with superhydrophobic surfaces as well as new insight into how interfacial shear stress may generate reverse flow in the contact line regions. The improved physical understanding of surface/interface effects on flow behavior on the nano- and microscale is essential for an accurate quantification of a wide variety of multiphase problems in porous media as well as for the design and manipulation of flow in microfluidics.

ASSOCIATED CONTENT

Supporting Information

Movie 1 shows colloid tracers in the contact line region moving in the direction opposite to bulk flow. This video recorded the flow in a 0.6 mm channel with a mean velocity of 0.514 mm s^{-1}. The derivation of the equation governing the static meniscus shape (eq 1) and its expression in the limit of very small channel width (eq 4) are shown. This material is available free of charge via the Internet at http://pubs.acs.org.

AUTHOR INFORMATION

Corresponding Author

*E-mail: yjin@udel.edu.

Notes

The authors declare no competing financial interest.

ACKNOWLEDGMENTS

We thank Dr. Kirk Czymmek and Dr. Jeffrey Caplan of the Delaware Biotechnology Institute's Bioimaging Center at the University of Delaware for training and assisting with confocal imaging and analysis. We gratefully acknowledge funding by the USDA National Research Initiative (NRI# 2008 - 00653) and the German Research Foundation DFG (MUSIS - FOR 1083).

REFERENCES

(1) Philip, J. R. Flow in Porous Media. *Annu. Rev. Fluid Mech.* **1970**, *2*, 177−204.

(2) Muccino, J. C.; Gray, W. G.; Ferrand, L. A. Toward an Improved Understanding of Multiphase Flow in Porous Media. *Rev. Geophys.* **1998**, *36*, 401−422.

(3) Gray, W. G.; Hassanizadeh, S. M. Averaging Theorems and Averaged Equations for Transport of Interface Properties in Multiphase Systems. *Int. J. Multiphase Flow* **1989**, *15*, 81−95.

(4) Atencia, J.; Beebe, D. J. Controlled Microfluidic Interfaces. *Nature* **2005**, *437*, 648−655.

(5) Gad-el-Hak, M. The Fluid Mechanics of Microdevices. The Freeman Scholar Lecture. *J. Fluid Eng.* **1999**, *121*, 5−33.

(6) Philip, J. R. Flows Satisfying Mixed No-Slip and No-Shear Conditions. *Z. Angew. Math. Phys.* **1972**, *23*, 353−372.

(7) Cottin-Bizonne, C.; Barentin, C.; Charlaix, E.; Bocquet, L.; Barrat, J. L. Dynamics of Simple Liquids at Heterogeneous Surfaces: Molecular-Dynamics Simulations and Hydrodynamic Description. *Eur. Phys. J. E* **2004**, *15*, 427−438.

(8) Lauga, E.; Stone, H. A. Effective Slip in Pressure-Driven Stokes Flow. *J. Fluid Mech.* **2003**, *489*, 55−77.

(9) Ybert, C.; Barentin, C.; Cottin-Bizonne, C.; Joseph, P.; Bocquet, L. Achieving Large Slip with Superhydrophobic Surfaces: Scaling Laws for Generic Geometries. *Phys Fluids* **2007**, *19*, 123601-1-10.

(10) Ayyaswam., Ps; Catton, I.; Edwards, D. K. Capillary Flow in Triangular Grooves. *J. Appl. Mech.* **1974**, *41*, 332−336.

(11) Romero, L. A.; Yost, F. G. Flow in an Open Channel Capillary. *J. Fluid Mech.* **1996**, *322*, 109−129.

(12) Parkinson, L.; Sedev, R.; Fornasiero, D.; Ralston, J. The Terminal Rise Velocity of 10−100 μm Diameter Bubbles in Water. *J. Colloid Interface Sci.* **2008**, *322*, 168−172.

(13) Wang, G. M.; Prabhakar, R.; Sevick, E. M., Hydrodynamic Mobility of an Optically Trapped Colloidal Particle near Fluid-Fluid Interfaces. *Phys. Rev. Lett.* **2009**, *103*, 248303-1-4.

(14) Chan, D. Y. C.; Manica, R.; Parkinson, L.; Ralston, J. Interpreting the Dynamic Interaction between a Very Small Rising Bubble and a Hydrophilic Titania Surface. *J. Phys. Chem. C* **2010**, *114*, 1942−1946.

(15) Manor, O.; Vakarelski, I. U.; Stevens, G. W.; Grieser, F.; Dagastine, R. R.; Chan, D. Y. C. Dynamic Forces between Bubbles and Surfaces and Hydrodynamic Boundary Conditions. *Langmuir* **2008**, *24*, 11533−11543.

(16) Yang, D.; Krasowska, M.; Priest, C.; Popescu, M. N.; Ralston, J. Dynamics of Capillary-Driven Flow in Open Microchannels. *J. Phys. Chem. C* **2011**, *115*, 18761−18769.

(17) Lazouskaya, V.; Jin, Y.; Or, D. Interfacial Interactions and Colloid Retention under Steady Flows in a Capillary Channel. *J. Colloid Interface Sci.* **2006**, *303*, 171−184.

(18) Manor, O.; Vakarelski, I. U.; Tang, X. S.; O'Shea, S. J.; Stevens, G. W.; Grieser, F.; Dagastine, R. R.; Chan, D. Y. C. Hydrodynamic Boundary Conditions and Dynamic Forces between Bubbles and Surfaces. *Phys. Rev. Lett.* **2008**, *101*, 024501.

(19) Ransohoff, T. C.; Radke, C. J. Laminar-Flow of a Wetting Liquid Along the Corners of a Predominantly Gas-Occupied Noncircular Pore. *J. Colloid Interface Sci.* **1988**, *121*, 392−401.

(20) Su, S. K.; Lai, C. L. Interfacial Shear-Stress Effects on Transient Capillary Wedge Flow. *Phys. Fluids* **2004**, *16*, 2033−2043.

(21) Tchikanda, S. W.; Nilson, R. H.; Griffiths, S. K. Modeling of Pressure and Shear-Driven Flows in Open Rectangular Microchannels. *Int. J. Heat Mass Trans.* **2004**, *47*, 527−538.

(22) Thomas, S. K.; Lykins, R. C.; Yerkes, K. L. Fully Developed Laminar Flow in Trapezoidal Grooves with Shear Stress at the Liquid-Vapor interface. *Int. J. Heat Mass Trans.* **2001**, *44*, 3397−3412.

(23) Tsai, P. C.; Peters, A. M.; Pirat, C.; Wessling, M.; Lammertink, R. G. H.; Lohse, D. Quantifying Effective Slip Length over Micropatterned Hydrophobic Surfaces. *Phys Fluids* **2009**, *21*, 112002.

(24) Steinberger, A.; Cottin-Bizonne, C.; Kleimann, P.; Charlaix, E. High Friction on a Bubble Mattress. *Nat. Mater.* **2007**, *6*, 665−668.

(25) Cottin-Bizonne, C.; Cross, B.; Steinberger, A.; Charlaix, E. Boundary Slip on Smooth Hydrophobic Surfaces: Intrinsic Effects and Possible Artifacts. *Phys. Rev. Lett.* **2005**, *94*, 056102.

(26) Vinogradova, O. I.; Koynov, K.; Best, A.; Feuillebois, F. Direct Measurements of Hydrophobic Slippage Using Double-Focus Fluorescence Cross-Correlation. *Phys. Rev. Lett.* **2009**, *102*, 118302.

(27) Santiago, J. G.; Wereley, S. T.; Meinhart, C. D.; Beebe, D. J.; Adrian, R. J. A Particle Image Velocimetry System for Microfluidics. *Exp Fluids* **1998**, *25*, 316−319.

(28) Happel, J.; Brenner, H. *Low Reynolds Number Hydrodynamics: With Special Applications to Particulate Media*; Prentice-Hall: Englewood Cliffs, NJ, 1965.

(29) Park, J. S.; Choi, C. K.; Kihm, K. D. Optically Sliced Micro-PIV Using Confocal Laser Scanning Microscopy (CLSM). *Exp. Fluids* **2004**, *37*, 105−119.

(30) Lindken, R.; Rossi, M.; Grosse, S.; Westerweel, J. Micro-Particle Image Velocimetry (μPIV): Recent developments, Applications, and Guidelines. *Lab Chip* **2009**, *9*, 2551−2567.

(31) Wan, J. M.; Tokunaga, T. K.; Tsang, C. F.; Bodvarsson, G. S. Improved Glass Micromodel Methods for Studies of Flow and Transport in Fractured Porous Media. *Water Resour. Res.* **1996**, *32*, 1955−1964.

(32) Yaminsky, V. V.; Ohnishi, S.; Vogler, E. A.; Horn, R. G. Stability of Aqueous Films between Bubbles. Part 1. The Effect of Speed on Bubble Coalescence in Purified Water and Simple Electrolyte Solutions. *Langmuir* **2010**, *26*, 8061−8074.

(33) Rothstein, J. P. Slip on Superhydrophobic Surfaces. *Annu. Rev. Fluid Mech.* **2010**, *42*, 89−109.

(34) Bird, R. B.; Stewart, W. E.; Lightfoot, E. N. *Transport Phenomena*, 2nd ed.; John Wiley: New York, 2002.

(35) Cheng, L. X.; Ribatski, G.; Thome, J. R. Two-Phase Flow Patterns and Flow-Pattern Maps: Fundamentals and Applications. *Appl. Mech. Rev.* **2008**, *61*, 050802.

(36) Chow, V. T. *Open-Channel Hydraulics*; McGraw-Hill: New York, 1959; pp 24−26.

(37) Francis, J. B. On the Cause of the Maximum Velocity of Water Flowing in Open Channels Being below the Surface. *Trans. Am. Soc. Civ. Eng.* **1878**, *23*, 120−130.

(38) Franzini, J. B.; Finnemore, E. J.; Daugherty, R. L. *Fluid Mechanics with Engineering Applications*, 9th ed.; McGraw-Hill: New York, 1997.

(39) Yuster, S. T. Theoretical Considerations of Multiphase Flow in Idealized Capillary Systems. *Proc. 3rd World Pet. Congr., The Hague* **1951**, 446−459.

(40) Miller, E. E.; Miller, R. D. Physical Theory for Capillary Flow Phenomena. *J. Appl. Phys.* **1956**, *27*, 324−332.